STRUCTURAL BIOLOGY

Stomatin encapsulates aquaporin-1 and urea transporter–B in the erythrocyte membrane

Francesca Vallese[1,2]*, Huan Li[3,4], Lucia Barazzuol[5], Tito Calì[5], Oliver B. Clarke[3,4]*

Stomatin is a ubiquitous and highly expressed protein in erythrocytes, which associates with cholesterol-rich microdomains in the plasma membrane and is known to regulate the activity of multiple ion channels and transporters, but the structural basis of association with stomatin targets remains unknown. Here, we describe high-resolution structures of multiple stomatin complexes with endogenous binding partners isolated from human erythrocyte membranes, revealing that stomatin specifically associates with two membrane proteins involved in water transport and cell volume regulation, aquaporin-1 and the urea transporter SLC14A1. Together, our results reveal the structural basis of stomatin oligomerization, membrane association, and target recruitment and identify a putative role for stomatin in the regulation of osmotic balance in the erythrocyte.

INTRODUCTION

Compartmentalization is a fundamental principle of cell biology, enabling the spatial separation of distinct metabolic pathways and control of the local solution conditions. Apart from membrane-bound organelles, compartmentalization can be achieved by the assembly of protein microcompartments such as encapsulins in bacteria and archaea (*1*), the soluble major vault protein in eukaryotes (*2*, *3*), and a broad class of membrane-associated oligomeric assemblies including homologs of stomatin, prohibitin, flotillin, and HflK/C, known as the SPFH superfamily.

The first and eponymous member of the SPFH family, stomatin was first identified in erythrocytes (where it is also known as band 7) and is expressed in many cell types and organisms (*4*). Stomatin deficiency has been linked to erythrocyte fragility and a condition called overhydrated hereditary stomatocytosis, in which erythrocytes leak Na^+ and K^+ ions (*5*). Since the identification of stomatin, numerous SPFH family members have been identified in all three domains of life. The conservation among these proteins is high, with human stomatin homologs sharing >50% identity (*6*). Despite being associated with a variety of diseases such as cancer, kidney failure, and anemia (*7*, *8*), the molecular functions of SPFH family members in most cases remain enigmatic.

SPFH proteins regulate various cellular processes across all domains of life, from bacteria to eukaryotes (*6*). Members of this family typically have a single transmembrane or intramembrane (TM/IM) segment that anchors the protein to the membrane, as well as a conserved pair of cytosolic SPFH1/2 domains that mediate, along with a pair of coiled-coil domains, the formation of pseudosymmetric dome-like assemblies (*9*, *10*). Bacterial SPFH proteins, such as HflK/C, are known to encapsulate target membrane proteins (e.g., the FtsH protease in the case of HflK/C) as part of their mechanism for regulating target protein function, but the extent to which this mechanism applies to eukaryotic SPFH proteins is unclear. Cryo–electron microscopy (cryo-EM) structures of several eukaryotic SPFH proteins, including an apo-structure of recombinant stomatin (*11*), were recently published (*12*), showing that while the dome architecture and domain arrangement are largely conserved, the size, stoichiometry, and interprotomer interfaces of the complex vary substantially between different family members.

Stomatin localizes to lipid rafts in the plasma membrane (*13*) and is enriched in extracellular vesicles, consistent with a role in membrane organization and cargo sorting (*14*, *15*). Functionally, stomatin and stomatin-like proteins have been implicated in channel/transporter modulation and mechanosensory pathways (*15*, *16*). Reported interactors include aquaporin-1 (AQP1), anion and cation channels [e.g., acid-sensing ion channels (ASICs)], pannexins, and glucose transporters (*17*, *18*), among others, though the molecular basis for these interactions has remained unclear.

Using single-particle cryo-EM, we have determined the architecture of stomatin complexes purified from native human erythrocyte membranes at an overall resolution of 2.0 Å. The stomatin oligomer forms a 16-subunit ring built from eight asymmetric homodimers, with C16/C8 mixed symmetry. We identify and characterize complexes with two endogenous partners, positioned beneath the dome, by using focused three-dimensional (3D) classification: an AQP1 tetramer and a urea transporter–B (UT-B) trimer surrounded by an encircling lipid belt. These data show that endogenous stomatin acts as a membrane scaffold that corrals and positions stomatin-associated membrane proteins, providing a structural framework for membrane protein microcompartmentalization at the erythrocyte plasma membrane.

RESULTS

Purification and structure determination of human stomatin complexes

Stomatin complexes were purified from digitonin-solubilized human erythrocyte membranes by the following strategy. First, high–molecular weight complexes (including the ankyrin complex and the stomatin complexes) were separated from lower–molecular weight species by glycerol density gradient centrifugation. The stomatin complexes were then separated from other contaminants by anion exchange, followed by size exclusion chromatography, to generate the final sample used for structural characterization (fig. S1). Initial

[1]Structural Biology Initiative, CUNY Advanced Science Research Center, New York, NY 10031, USA. [2]Department of Chemistry and Biochemistry, City College of New York, New York, NY 10031, USA. [3]Department of Anesthesiology, Columbia University Irving Medical Center, New York, NY 10032, USA. [4]Department of Physiology and Cellular Biophysics, Columbia University, New York, NY 10032, USA. [5]Department of Biomedical Sciences, University of Padua, Padua, Italy.
*Corresponding author. Email: fvallese@gc.cuny.edu (F.V.); olibclarke@gmail.com (O.B.C.)

structural characterization of the digitonin-solubilized stomatin complex revealed an apparently C16 symmetric, dome-shaped assembly, with a partially membrane-embedded N-terminal SPFH1 domain (fig. S2A). Featureless β strands on the inner wall of the apical cap region led us to suspect the presence of pseudosymmetry, and focused classification without alignments allowed us to identify the overall symmetry as C8 (fig. S3), with eight asymmetric homodimers forming the 16-protomer assembly. Refinement in C8 resulted in a reconstruction with an overall resolution of 2.0 Å and facilitated building a near-complete model of human stomatin (Fig. 1), including multiple palmitoylation sites in the membrane-embedded region.

Architecture and pseudosymmetry of the stomatin dome

The cryo-EM reconstruction reveals a dome-shaped 16-subunit ring assembled from eight asymmetric homodimers, with C16/C8 mixed symmetry (Fig. 2A). The membrane-proximal base is formed by an SPFH1 domain and an intramembrane helix (IMH1; residues ~20 to 53) contributed by each protomer, which together define the base of the dome and exhibit C16 symmetry (fig. S2A). The cytosolic SPFH2 domains form a second layer of interactions at the base of the dome, followed by the first coiled-coil (CC1) domains, which arch upward to an apical cap (distal to the membrane), formed by the second coiled-coil domain (CC2) and the C-terminal β strand (β-Ct). The β-Ct strand forms a 16-stranded β barrel, in which every adjacent strand (contributed alternately by the A and B protomers) is offset in sequence register with respect to its neighbor by one residue (Fig. 2B). This register shift breaks the C16 symmetry of the assembly, yielding C8 symmetry in the C-terminal region. Thus, the assembly displays mixed C16/C8 symmetry—C16 for the SPFH1 and 2 ring and C8 for the Ct β barrel and surrounding interacting regions. At 2.0 Å overall resolution, side chains and solvent molecules are well resolved throughout the dome and intramembrane belt (fig. S2D and movies S1 and S2). The only poorly ordered region is the very N terminus, where lower-contour views reveal weak density for the first ~20 residues that bind to the SPFH1/2 interdomain interface. The base spans ~140 Å outer diameter; the SPFH belt widens to ~160 Å before tapering toward the apex, yielding a dome height of ~100 Å. A continuous axial pore runs through the assembly and narrows to a ~7.3-Å final radius in the C-terminal β barrel (fig. S2C), which is lined almost exclusively by hydrophobic residues (Fig. 2B and fig. S2B). The top pore remains open, showing only faint density and a few unmodeled C-terminal residues, with no ordered plug, suggesting the possibility that this aperture may be permeable to solvent (fig. S2E). Contiguous density is observed protruding from the side chains of Cys^{30}, Cys^{53}, and Cys^{87}, compatible with S-palmitoylation (Fig. 2C and fig. S4). This is consistent with prior literature for Cys^{30} and Cys^{87} (*19*, *20*), and we now see analogous density at Cys^{53}, suggesting possible palmitoylation of this residue as well. Together, these modifications could help anchor the complex in lipid rafts and promote stability of the dome. A local asymmetric refinement of the membrane-embedded region also allows us to identify multiple noncovalently bound phospholipids, one of which is consistent with sphingosine-1-phosphate (Fig. 2D). Perhaps unexpectedly given the association of stomatin with cholesterol-rich domains in the membrane, no ordered cholesterol molecules are identified binding to the stomatin intramembrane region. In the C-terminal cytosolic β barrel, eight nonprotein densities are found lining the hydrophobic

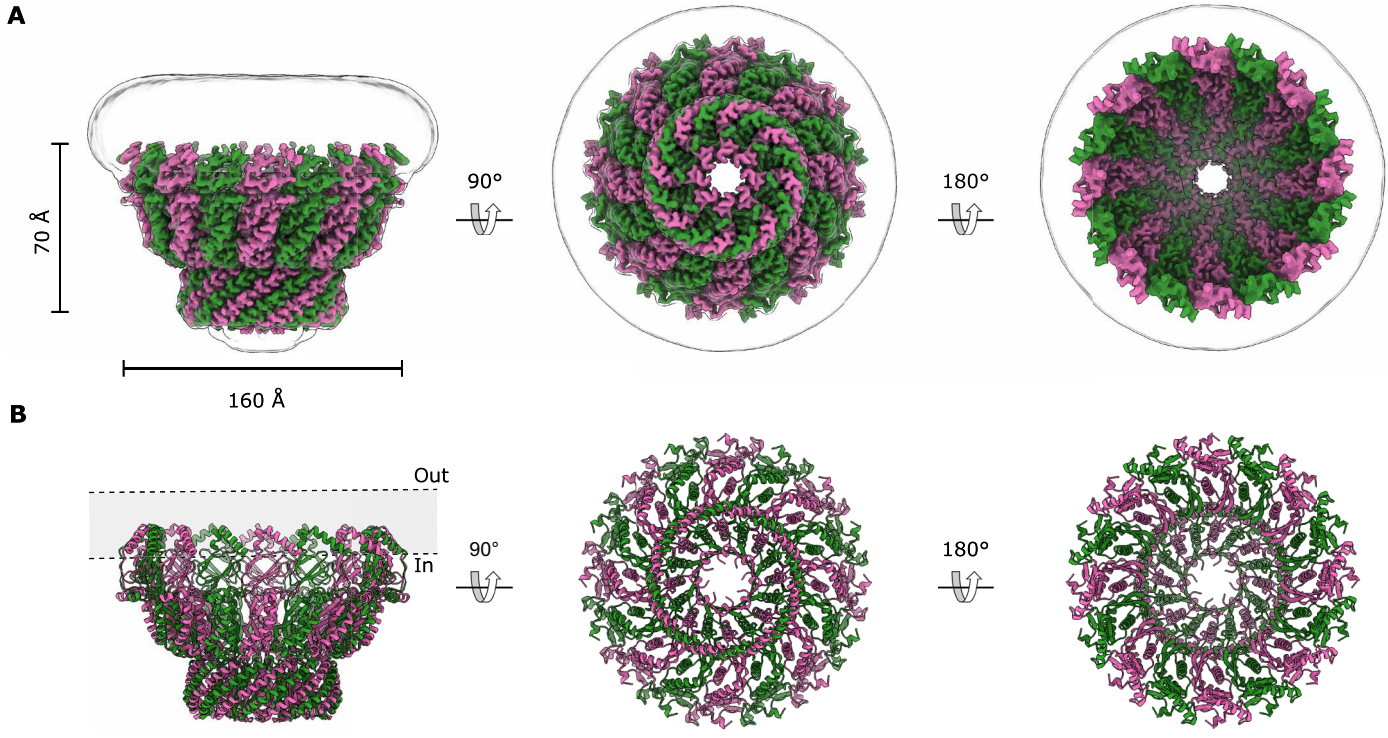

Fig. 1. Architecture of human stomatin. (**A**) Cryo-EM density map (EMD-73881) of stomatin viewed in the membrane plane (left), from the cytoplasmic side (center), and the extracellular side (right). The 16 stomatin protomers are alternately colored pink (protomer A) and green (protomer B). The Gaussian-filtered map is shown as a transparent surface to delineate the boundaries of the micelle. (**B**) Atomic model of stomatin, shown in the same orientations and color scheme as in (A).

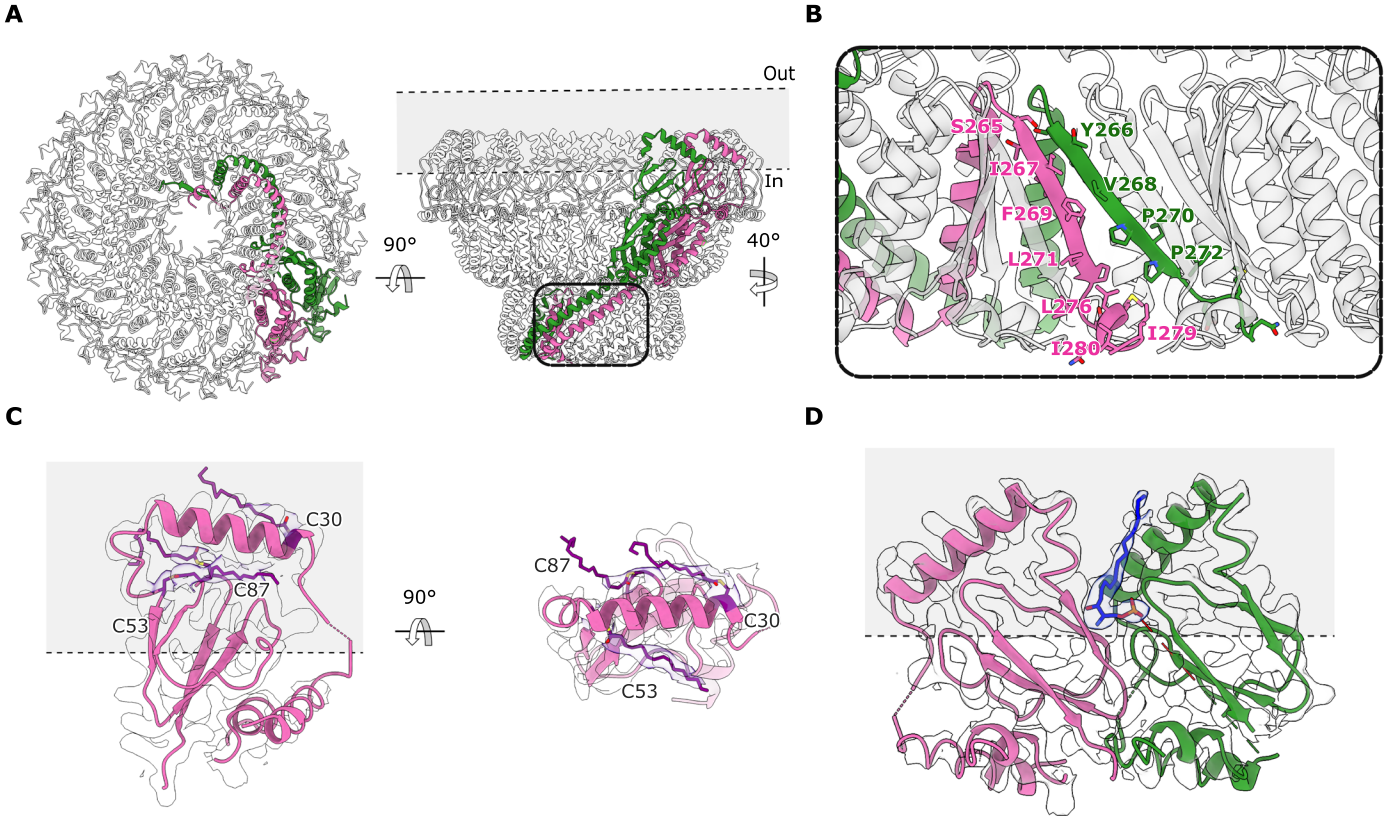

Fig. 2. Structural features of stomatin. (**A**) Model of stomatin with one of the eight dimers highlighted (pink and green for stomatin protomers A and B, respectively), viewed from the cytoplasmic side (left) and in the membrane plane (right). (**B**) Close-up view of the stomatin apical C-terminal β barrel, showing residues that line the internal pore. (**C**) Atomic model of the SPFH1 domain and IMH1/2 region of stomatin protomer A viewed in the membrane plane, with putative palmitoylation sites on Cys^{30}, Cys^{53}, and Cys^{87} highlighted in purple, and the cryo-EM density map shown as a transparent surface (EMD-74052). (**D**) Model of the intramembrane region of a dimer, with the sphingosine-1-phosphate modeled between the monomers shown in blue.

aperture. The shapes of these densities (fig. S2E) are inconsistent with cholesterol or digitonin and are more reminiscent of free fatty acids, although their precise identity cannot be determined unambiguously.

Identification of endogenous stomatin binding partners by deep 3D classification

Filtering the C8 or C16 reconstructions to low resolution revealed strong but uninterpretable density in the center of the digitonin micelle, leading us to suspect the presence of stomatin binding partners under the dome. Classification of asymmetric transmembrane binding partners associating with a highly symmetric, but flexible assembly is a challenging image processing task, and initial classification attempts using multiple different approaches failed or gave ambiguous results. Focused classification without alignments using an unusually large number of 3D classes (which we are terming here deep 3D classification) at low resolution (12 to 15 Å) succeeded in identifying two main populations of stomatin-encapsulated membrane proteins—one with apparent local C4 symmetry, and another with apparent C3 symmetry (figs. S5 and S6). Local refinement with the apparent local symmetry enforced facilitated high-resolution reconstructions of both species, identifying the former as AQP1, resolved at 2.3 Å, and the latter as the urea transporter UT-B, resolved at 2.8 Å (Fig. 3) (*16*, *18*). On the basis of analysis of the classification results, approximately 40% of stomatin domes are associated with AQP1, 10% are associated with UT-B, and 50% are empty or have inconclusive density. AQP1 is positioned asymmetrically within the stomatin dome, interacting directly with the inner portion of the intramembrane domain (fig. S7, A and B), while the UT-B trimer is positioned in the center of the stomatin dome, interacting with stomatin via lipid-mediated interactions (fig. S7C).

Architecture of the AQP1 and UT-B stomatin complexes

A single AQP1 tetramer is located within the membrane patch defined by the stomatin dome, interacting with the wall of the dome, primarily with IMH2 (Fig. 3, A and B, and fig. S7, A and B). No classes were identified with multiple AQP1 tetramers. Each AQP1 monomer contains a single water pore, so the tetramer harbors four independent water pathways. As identified in the structure of ankyrin-bound AQP1 (*21*), Cys^{87} of AQP1 is palmitoylated and a bound cholesterol molecule is observed near the intracellular interprotomer interface. In the stomatin-AQP1 structure, the tetramer sits off-axis relative to the assembly's pseudo-C16 symmetry axis and engages the intramembrane surfaces of two stomatin protomers belonging to adjacent dimers (fig. S7B). The stomatin intramembrane belt forms a continuous ring that surrounds AQP1, effectively sequestering it from the surrounding bilayer and limiting lateral diffusion outside of the lumen. The protein-protein interface is limited, probably confined to AQP1 cytosolic loops and termini (fig. S7, A

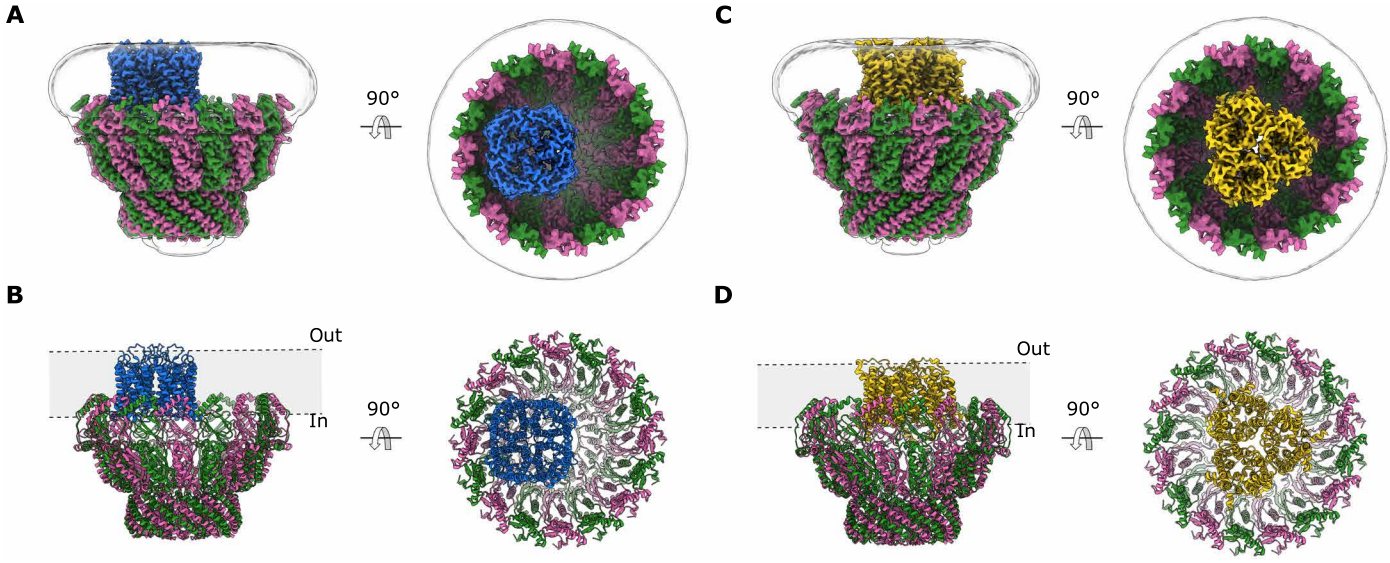

Fig. 3. Structural identification of AQP1 and UT-B as stomatin-associated membrane proteins. (**A**) Cryo-EM density map of stomatin in pink and green (EMD-73881) in complex with AQP1 in blue (EMD-74046), viewed in the membrane plane (left) and from the extracellular side (right). The Gaussian-filtered map delineating the micelle boundary is shown as a transparent white surface. (**B**) Atomic model of the stomatin-AQP1 complex, shown in the same orientations and color scheme as in (A). (**C**) Cryo-EM density map of stomatin in pink and green (EMD-73881) in complex with UT-B in yellow (EMD-74047), viewed in the membrane plane (left) and from the extracellular side (right). (**D**) Atomic model of the stomatin–UT-B complex, shown in the same orientations and color scheme as in (C).

and B); the water pore remains fully resolved and unobstructed in each monomer.

3D classification also revealed a second partner within the dome: the urea transporter UT-B (SLC14A1) (Fig. 3, C and D). In contrast to AQP1, the homotrimeric UT-B transporter is positioned in the center of the dome, with each subunit contributing 10 transmembrane helices and the trimer presenting its characteristic triangular footprint to the membrane. We observe a continuous annulus of density surrounding the UT-B transmembrane surface (fig. S7C). Although we cannot unequivocally assign the outer lipids, they form a "lipid belt" that seems to bridge UT-B to the inner face of the stomatin intramembrane ring, providing lipid-mediated contacts in the membrane plane. We do not resolve direct polypeptide-polypeptide contacts between UT-B and stomatin within the bilayer, with all contacts appearing to be lipid mediated. The geometry and location of many of the phospholipids that directly contact UT-B match those reported in recent human UT-B/UT-A structures, where lipids occupy defined grooves between subunits (*22*). Lipidomics of the UT-B, which was used for prior structure determination by Chi *et al.* (*22*), reported two main lipid species—phosphatidylethanolamine and phosphatidylinositol. However, because our samples derive from native erythrocyte membranes, we cannot exclude the presence of different lipids, and the quality of the lipid densities is insufficient to assign the headgroups unambiguously.

DISCUSSION

Our structures define stomatin as a dome-shaped, C16/C8 pseudo-symmetric assembly that corrals specific membrane proteins within a membrane patch under the stomatin dome. Two native stomatin-associated membrane proteins, AQP1 and UT-B, sit inside the intramembrane belt beneath the dome, providing a direct structural basis for stomatin-dependent regulation of water and urea transport in the erythrocyte membrane, processes critical for regulation of osmotic balance and cell volume (*23*, *24*). Beyond erythrocytes, these data support a general model in which SPFH oligomers build membrane-bound microcompartments that couple tuning of local lipid composition to cargo selection and function. An analogous "membrane-encapsulin" role has been characterized in bacteria, where the SPFH pair HflK/C assemble a ring that corrals multiple FtsH proteases into a microcompartment, spatially organizing proteolysis at the membrane (*25*).

SPFH proteins all have a single intramembrane or transmembrane segment and a conserved pair of SPFH1 and SPFH2 domains, yet their higher-order architectures are diverse (fig. S8). Stomatin forms a ~160-Å dome from eight asymmetric homodimers, with a narrow, hydrophobic apical pore and a continuous intramembrane belt. Differences in ring diameter, pore geometry, and belt topology (which can be transmembrane or intramembrane), as well as the lipid composition of the host membrane, likely tune the cargo selectivity of different SPFH family members.

Deep 3D classification of native stomatin, purified from human erythrocytes, resolved two stomatin-cargo complexes, with AQP1 and UT-B, demonstrating that stomatin accommodates cargos of distinct symmetry and interaction modes, which may be direct (AQP1) or lipid mediated (UT-B). Characterization of the stomatin-AQP1 and stomatin–UT-B complexes extends the encapsulin principle to the eukaryotic plasma membrane, with the stomatin oligomer forming a palmitoylated fence that isolates cargos in raft-like regions and dampens their lateral mobility. The deep 3D classification approach we have applied here to stomatin may help resolve the cargo of other native SPFH complexes for which data are available, such as the flotillin1/2 complex. It is unclear whether encapsulation is the only mechanism by which stomatin regulates cargo proteins, or whether other target proteins may associate with the outer surface of the dome. The hydrophobic apical pore, which we see here, is

decorated by small amphiphiles and likely forms a conduit for the transport substrates of the resident membrane proteins, although it remains possible, depending on the conformation of the unresolved C termini, that the cap may seal off the cargo membrane protein from the surrounding solvent, either temporarily/dynamically or permanently (Fig. 4).

While the structural basis for stomatin association with target membrane proteins, and the identity of two of them, is now clear, several questions remain to be answered regarding the mechanistic basis and functional consequences of this process. First, questions surround the timing and dynamics of stomatin complex assembly. Erythrocytes do not have ribosomes [or if they do, they exist at a very low level for specialized purposes (*26*)], so when are the stomatin domes being assembled around target proteins? If it is happening in the mature erythrocyte, this implies the existence of a pool of partially assembled or disassembled stomatin domes, either in the cytosol or at the membrane, which can facilitate the entry of AQP1 or UT-B. Alternatively, it is possible that stomatin-encapsulated membrane proteins are assembled cotranslationally, during erythrocyte biogenesis, and perhaps the stomatin dome is then degraded by erythrocytic proteasomes (*27*) during erythrocyte aging (*28*), releasing target membrane proteins. In terms of the functional consequences of stomatin association, some clues exist, although no definitive answers are yet available. First, during overhydrated hereditary stomatocytosis, which is caused by mutations not in stomatin, but in the heterotrimeric ammonia transporter Rh-associated glycoprotein (RhAG) (*29*), stomatin is initially present, in young erythrocytes, at near-normal levels, but it is progressively lost during erythrocyte aging (*30*). Second, high levels of stomatin, along with stomatin-associated membrane proteins, are known to be present in extracellular vesicles, which are secreted from erythrocytes during aging or blood storage (*31*). These two observations, together, suggest a possible role for stomatin in sequestering and/or disposing of unneeded or damaged targeted membrane proteins. Nevertheless, the original *Stom*$^{-/-}$ mouse model showed no apparent erythrocyte phenotype (*32*), and subsequent context-specific studies [anesthetic sensitivity (*33*), burn-induced vascular injury (*34*), and bone remodeling (*35*)] indicate that stomatin plays modulatory roles. Future studies could include targeted red blood cell (RBC) assays of cation/volume homeostasis, membrane microdomain organization, and stress-evoked deformability/osmotic fragility, which may uncover phenotypes consistent with our AQP1/UT-B model.

Erythrocytes experience extreme mechanical stress and rapid osmotic shifts yet lack endomembranes and transcriptional plasticity, necessitating alternative methods to control membrane transport processes. Stomatin provides (i) compartmentalized control of water and urea flux via AQP1 and UT-B, (ii) possible stabilization of raft architecture, and (iii) a sorting platform that can be shed in extracellular vesicles during blood aging or storage (Fig. 4), together offering a plausible basis for coordinated water/urea handling in circulation.

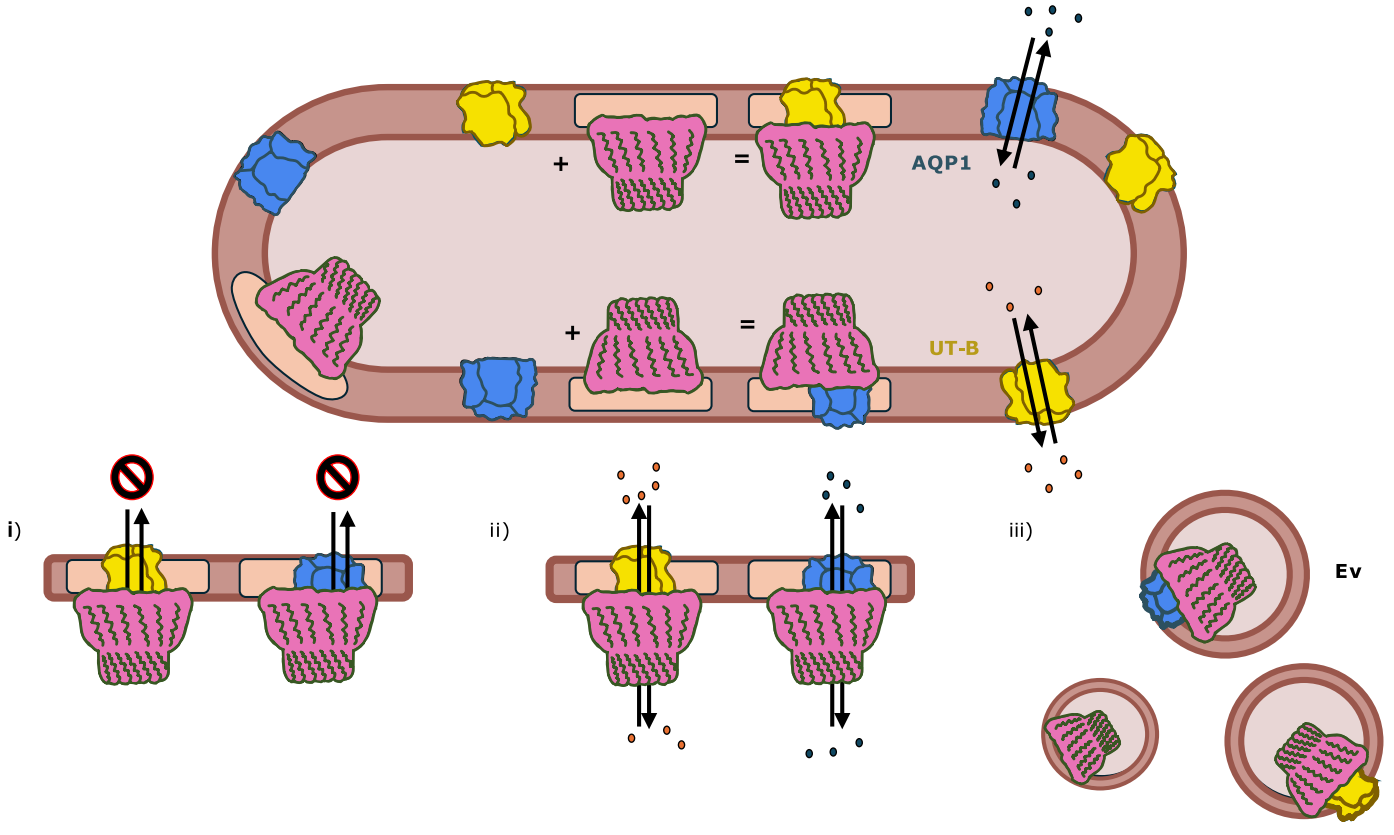

Fig. 4. Schematic of the human stomatin in erythrocytes. Illustration of the possible functions of stomatin complex formation with AQP1 (blue) and UT-B (yellow) in erythrocytes. Beige shading in the membrane indicates microdomains. Stomatin may regulate AQP1 and UT-B in several ways: (**i**) blocking substrate exchange, water for AQP1 and urea for UT-B; (**ii**) capping the proteins to modulate substrate flux by restricting flow of substrates into and out of the stomatin dome; and (**iii**) promoting removal of cargo proteins from the plasma membrane via extracellular vesiculation.

MATERIALS AND METHODS

Stomatin sample preparation for cryo-EM

The general purification workflow is presented in fig. S1. Erythrocyte ghost membranes were prepared as described by Niggli and Carafoli (*36*). Briefly, red blood cells from healthy blood donors were purchased from the New York Blood Center. Erythrocytes were washed twice in 5 volumes of 130 mM KCl and 10 mM tris-HCl (pH 7.4). The cells were hemolyzed in 5 volumes of 1 mM EDTA and 10 mM tris-HCl (pH 7.4), and centrifuged at 18,000*g* for 10 min. The resulting ghost membranes were then washed five times in the hemolysis buffer and four additional times in 10 mM Hepes (pH 7.4). The hemoglobin-free ghost membranes were lastly resuspended in 130 mM NaCl, 20 mM Hepes (pH 7.4), 0.5 mM $MgCl_2$, 0.05 mM $CaCl_2$, and 2 mM dithiothreitol, and stored at −80°C.

Ghost membranes were solubilized at a protein concentration of 4 mg/ml in 130 mM KCl, 10 mM Hepes (pH 7.4), protease inhibitor tablet (cOmplete, EDTA-free Protease Inhibitor Cocktail, Millipore Sigma), and 1% (w/v) digitonin (Carbosynth), at 4°C for 1 hour. Unsolubilized material was removed by centrifugation at 26,000*g* for 30 min. The supernatant was applied to a PD10 column (to reduce the detergent concentration) equilibrated with 0.05% (w/v) digitonin, 130 mM KCI, and 20 mM Hepes (pH 7.4). The sample was then applied on a glycerol step gradient (30 to 12% glycerol) and centrifuged for 15 hours at 25,000 rpm (SW 32 rotor, Beckman). The distribution of stomatin was confirmed by SDS–polyacrylamide gel electrophoresis gel (4 to 20% Mini-PROTEAN TGX Precast Protein Gels, Bio-Rad). Fractions containing stomatin were pooled together and concentrated to <500 μl using a 100-kDa cutoff concentrator. To further purify the sample, it was loaded onto a Superose 6 10/300 Increase column (Cytiva) equilibrated in 0.05% (w/v) digitonin, 130 mM KCl, and 20 mM Hepes (pH 7.4). Fractions enriched in stomatin were pooled and concentrated to 1 ml. The sample was then applied to a PD10 column equilibrated with 0.05% (w/v) digitonin and 20 mM tris-HCl (pH 6.5) and subsequently loaded onto a 5-ml HiTrap ANX FF column (GE Healthcare). Proteins were eluted from the column with a step gradient of 0 to 0.6 M KCl in the same buffer (0.15, 0.3, and 0.6 M). The fractions from the 0.3 M KCl elution containing stomatin were collected and concentrated to ∼<500 μl using a 100-kDa cutoff concentrator (Millipore). The concentrated sample was further subjected to size exclusion chromatography on a Superose 6 10/300 column (GE HealthCare) equilibrated with 0.05% (w/v) digitonin, 130 mM KCI, and 20 mM Hepes (pH 7). The fraction enriched in stomatin was immediately used for cryo-EM grid preparation.

Cryo-EM grid preparation and data collection

Purified stomatin (3 μl) at 4 mg/ml with a surface-active additive [0.01% (w/v) glycyrrhizic acid; Thermo Fisher Scientific] (*21*) was added to a glow-discharged (PELCO easiGlow) 0.6/1 μm holey gold grid (Quantifoil UltrAuFoil) and blotted for 4 to 6 s at 4°C and 100% humidity using the Vitrobot Mark IV system (Thermo Fisher Scientific), before plunging immediately into liquid ethane for vitrification. The cryo-EM data were collected on a Titan Krios electron microscope (Thermo Fisher Scientific) equipped with a K3 direct electron detector (Gatan) operating at 0.83 Å per pixel in counting mode using Leginon automated data collection software (*37*, *38*). Data collection was performed using a dose of 58 $e^-/Å^2$ across 50 frames (50 ms per frame) at a dose rate of 16 e^-/pixel per second, using a set defocus range of −0.5 to −1.5 μm. A 100-μm objective aperture was used. A total of 20,647 micrographs were collected.

Cryo-EM data processing

Preprocessing, initial volume generation, and C16 consensus refinement

The final cryo-EM data processing workflow is summarized in fig. S3. Orientation distributions, Fourier shell correlation (FSC) plots, and validation statistics are presented in figs. S9 to S11 and table S1. Maps and masks have been deposited at Electron Microscopy Data Bank (EMDB) (see table S1). Subsequent steps were performed in cryoSPARC v4.4-4.71 unless otherwise indicated (*39*).

Patch-based motion correction and dose weighting of 20,647 movies were carried out in cryoSPARC using the Patch Motion job type. Patch-based contrast transfer function (CTF) estimation was performed on the aligned, non–dose-weighted averages using Patch CTF. Particles were manually picked from 93 micrographs. Topaz was run in training mode using a downsampling factor of 10 and an estimated number of particles per micrograph of 50. The resulting model was used to pick particles from the entire dataset using Topaz Extract. Approximately 592,000 particles were initially extracted in a box of 512 pixels and Fourier cropped to 96 pixels. Multiple rounds of 2D classification were performed to isolate homogeneous subsets of particles to use for ab initio reconstruction. Heterogeneous ab initio reconstruction was performed on approximately 355,000 particles selected by 2D classification, first without symmetry and then, after testing multiple different Cn symmetry groups, with C16 symmetry, which gave a map with clear secondary structural features. An initial refinement was performed using nonuniform refinement (*40*) (with C16 symmetry enforced) with on-the-fly refinement of per-particle defocus, and global refinement of beam tilt and trefoil aberrations, resulting in an initial consensus refinement with a resolution of 1.9 Å. Reference-based motion correction improved resolution in C16 to 1.84 Å.

C8 symmetry determination using 3D classification

In the C16 consensus nonuniform refinement map, the interior of the apex of the stomatin cap appeared poorly resolved, with no side-chain detail, while the immediately surrounding regions exhibited excellent density quality, leading us to suspect the presence of unresolved pseudosymmetry. To resolve the suspected pseudosymmetry in this region, a local mask covering this region was generated using UCSF ChimeraX (*41*–*43*) and CryoSPARC (*39*). Focused 3D classification on the cap region without alignments in C1 revealed two C8-symmetric classes related by a rotation around the Cn axis. The classes were aligned using Align 3D maps in CryoSPARC, updating particle alignments accordingly, and subjected to local refinement using a global mask, with C8 symmetry enforced, resulting in a reconstruction with a resolution of 1.9 Å. The membrane-embedded and membrane-proximal regions of stomatin remained less well resolved than the rest of the oligomer, likely due to continuous deformation of the stomatin cap, as assessed by both 3D Variability Analysis and 3D classification with a ring-shaped mask covering the membrane-embedded region of stomatin (fig. S3). To obtain a map that allowed confident model building in the membrane-embedded portion, another round of 3D classification with a mask around the stomatin membrane-embedded region allowed the identification of a set of approximately 38,000 particles with improved density for the intramembrane region, resulting in a 2.0-Å map after refinement

with C8 symmetry enforced, with well-defined density for the intramembrane helix, palmitoylation sites, and bound lipids. To analyze the stomatin intramembrane region, we applied C8 symmetry expansion to the initial C8-refined particles. After recentering the particles, we performed two local refinements: one with a larger soft mask covering an extended area that includes the intramembrane region and the SPFH1/2 domains, followed by one with a mask limited to the intramembrane region and the SPFH1 domain. We obtained a 2.4-Å map (EMD-74052) with improved density for the intramembrane region (fig. S3)

Identification of AQP1 and UT-B using deep 3D classification

To identify putative stomatin-associated membrane proteins, we applied 3D classification with 80 classes on a C16 symmetry–expanded particle set using a featureless, disk-shaped mask centered on the membrane-embedded region, with a target resolution of 12 Å (fig. S5). Different numbers of classes were tested, and a number of classes greater than 40 was found to be necessary to separate the bound membrane proteins. This analysis revealed two main binding partners present in distinct complexes: tetrameric AQP1 and trimeric UT-B. An overview of all 80 classes is shown in fig. S6. Classes corresponding to the two different binding partners were visually identified (fig. S6), and particles from the respective classes were then combined. After aligning the rotationally related classes and modifying the particle orientations accordingly, local refinement was used in two stages to improve the density for AQP1 and UT-B, initially in C1, and then by applying the local molecular symmetry—C4 symmetry for AQP1 and C3 symmetry for UT-B, resulting in maps at 2.3 and 2.8 Å resolution, respectively. To resolve the stomatin-AQP1 interface, we performed local asymmetric refinement starting from the initial postclassification reconstruction. A soft mask was generated to include the two AQP1 monomers in direct contact with stomatin, together with the four adjacent stomatin intramembrane domains. Local refinement was performed without symmetry enforced to improve the density at the AQP1-stomatin interface, resulting in a 3.1-Å map (EMD-74049) with improved density for the contact region.

Atomic model building and refinement

An initial model for the stomatin protomer was generated using AlphaFold 2 (*44*). An AQP1 structure (*21*) [Protein Data Bank (PDB) 7UZE] and UT-B structure (*22*) (PDB 8XDF) were used as initial models for building the corresponding proteins. Initial models were placed in corresponding local reconstructions and fit as rigid bodies using fitmap in UCSF Chimera (*45*). Each model was then manually extended and completed in COOT (*46*). Residues 5 to 22 of stomatin were assigned as unknown residues to indicate that the sequence register in this region is ambiguous. Waters and ligands were placed where justified by the density and chemical environment, and each final model was refined against the respective map using phenix.real_space_refine (*47*). An overview of the model-density fit for the different structures is provided in fig. S4. Figures were prepared using UCSF ChimeraX (*41*–*43*). Refinement and validation statistics are provided in table S1. Model map FSCs in table S1 were calculated with phenix.mtriage (*48*).

Supplementary Materials

The PDF file includes:
Figs. S1 to S11
Table 1
Legends for movies S1 and S2

Other Supplementary Material for this manuscript includes the following:
Movies S1 and S2

REFERENCES

1. B. J. LaFrance, C. Cassidy-Amstutz, R. J. Nichols, L. M. Oltrogge, E. Nogales, D. F. Savage, The encapsulin from *Thermotoga maritima* is a flavoprotein with a symmetry matched ferritin-like cargo protein. *Sci. Rep.* **11**, 22810 (2021).
2. N. L. Kedersha, L. H. Rome, Preparative agarose gel electrophoresis for the purification of small organelles and particles. *Anal. Biochem.* **156**, 161–170 (1986).
3. L. B. Kong, A. C. Siva, L. H. Rome, P. L. Stewart, Structure of the vault, a ubiquitous celular component. *Structure* **7**, 371–379 (1999).
4. C. M. Hiebl-Dirschmied, G. R. Adolf, R. Prohaska, Isolation and partial characterization of the human erythrocyte band 7 integral membrane protein. *Biochim. Biophys. Acta* **1065**, 195–202 (1991).
5. S. Rungaldier, E. Umlauf, M. Mairhofer, U. Salzer, C. Thiele, R. Prohaska, Structure-function analysis of human stomatin: A mutation study. *PLOS ONE* **12**, e0178646 (2017).
6. J. B. Green, J. P. W. Young, Slipins: Ancient origin, duplication and diversification of the stomatin protein family. *BMC Evol. Biol.* **8**, 44 (2008).
7. D. Wang, R. Tabti, S. Elderwish, A. Djehal, N. Chouha, F. Pinot, P. Yu, C. G. Nebigil, L. Désaubry, SFPH proteins as therapeutic targets for a myriad of diseases. *Bioorg. Med. Chem. Lett.* **30**, 127600 (2020).
8. N. I. A. Rahman, A. Sato, K. Tsevelnorov, A. Shimizu, M. Komeno, M. K. B. Ahmat Amin, M. R. Molla, J. E. C. Soh, L. K. C. Nguyen, A. Wada, A. Kawauchi, H. Ogita, Stomatin-mediated inhibition of the Akt signaling axis suppresses tumor growth. *Cancer Res.* **81**, 2318–2331 (2021).
9. Z. Qiao, T. Yokoyama, X.-F. Yan, I. T. Beh, J. Shi, S. Basak, Y. Akiyama, Y.-G. Gao, Cryo-EM structure of the entire FtsH-HflKC AAA protease complex. *Cell Rep.* **39**, 110890 (2022).
10. C. Ma, C. Wang, D. Luo, L. Yan, W. Yang, N. Li, N. Gao, Structural insights into the membrane microdomain organization by SPFH family proteins. *Cell Res.* **32**, 176–189 (2022).
11. J. Stoner, S. Li, Z. Fu, Structural basis for membrane microdomain formation by a human stomatin complex. *Nat. Commun.* **16**, 7439 (2025).
12. Z. Fu, R. MacKinnon, Structure of the flotillin complex in a native membrane environment. *Proc. Natl. Acad. Sci. U.S.A.* **121**, e2409334121 (2024).
13. U. Salzer, R. Prohaska, Stomatin, flotillin-1, and flotillin-2 are major integral proteins of erythrocyte lipid rafts. *Blood* **97**, 1141–1143 (2001).
14. T. Bebesi, D. Kitka, A. Gaál, I. C. Szigyártó, R. Deák, T. Beke-Somfai, K. Koprivanacz, T. Juhász, A. Bóta, Z. Varga, J. Mihály, Storage conditions determine the characteristics of red blood cell derived extracellular vesicles. *Sci. Rep.* **12**, 977 (2022).
15. G. O. Skryabin, A. V. Komelkov, S. A. Galetsky, D. V. Bagrov, E. G. Evtushenko, I. I. Nikishin, K. I. Zhordaniia, E. E. Savelyeva, M. E. Akselrod, I. G. Paianidi, E. M. Tchevkina, Stomatin is highly expressed in exosomes of different origin and is a promising candidate as an exosomal marker. *J. Cell. Biochem.* **122**, 100–115 (2020).
16. S. Genetet, A. Desrames, Y. Chouali, P. Ripoche, C. Lopez, I. Mouro-Chanteloup, Stomatin modulates the activity of the anion exchanger 1 (AE1, SLC4A1). *Sci. Rep.* **7**, 46170 (2017).
17. J. Z. Zhang, W. Abbud, R. Prohaska, F. Ismail-Beigi, Overexpression of stomatin depresses GLUT-1 glucose transporter activity. *Am. J. Physiol. Cell Physiol.* **280**, C1277–C1283 (2001).
18. S. Rungaldier, W. Oberwagner, U. Salzer, E. Csaszar, R. Prohaska, Stomatin interacts with GLUT1/SLC2A1, band 3/SLC4A1, and aquaporin-1 in human erythrocyte membrane domains. *Biochim. Biophys. Acta* **1828**, 956–966 (2013).
19. L. Snyers, E. Umlauf, R. Prohaska, Cysteine 29 is the major palmitoylation site on stomatin. *FEBS Lett.* **449**, 101–104 (1999).
20. I. C. Morrow, S. Rea, S. Martin, I. A. Prior, R. Prohaska, J. F. Hancock, D. E. James, R. G. Parton, Flotillin-1/reggie-2 traffics to surface raft domains via a novel golgi-independent pathway. Identification of a novel membrane targeting domain and a role for palmitoylation. *J. Biol. Chem.* **277**, 48834–48841 (2002).
21. F. Vallese, K. Kim, L. Y. Yen, J. D. Johnston, A. J. Noble, T. Calì, O. B. Clarke, Architecture of the human erythrocyte ankyrin-1 complex. *Nat. Struct. Mol. Biol.* **29**, 706–718 (2022).
22. G. Chi, L. Dietz, H. Tang, M. Snee, A. Scacioc, D. Wang, G. Mckinley, S. M. M. Mukhopadhyay, A. C. W. Pike, R. Chalk, N. A. Burgess-Brown, J.-P. Timmermans, W. van Putte, C. V. Robinson, K. L. Dürr, Structural characterization of human urea transporters UT-A and UT-B and their inhibition. *Sci. Adv.* **9**, eadg8229 (2023).
23. J. Sugie, M. Intaglietta, L. A. Sung, Water transport and homeostasis as a major function of erythrocytes. *Am. J. Physiol. Heart Circ. Physiol.* **314**, H1098–H1107 (2018).
24. S. Azouzi, M. Gueroult, P. Ripoche, S. Genetet, Y. Colin Aronovicz, C. Le Van Kim, C. Etchebest, I. Mouro-Chanteloup, Energetic and molecular water permeation mechanisms of the human red blood cell urea transporter B. *PLOS ONE* **8**, e82338 (2013).
25. O. Daumke, G. R. Lewin, SPFH protein cage—One ring to rule them all. *Cell Res.* **32**, 117–118 (2022).
26. S. D. Kumar, D. Kar, M. N. Akhtar, B. Willard, D. Roy, T. Hussain, P. I. Rajyaguru, S. M. Eswarappa, Evidence for low-level translation in human erythrocytes. *Mol. Biol. Cell* **33**, br21 (2022).

27. W. Sae-Lee, C. L. McCafferty, E. J. Verbeke, P. C. Havugimana, O. Papoulas, C. D. McWhite, J. R. Houser, K. Vanuytsel, G. J. Murphy, K. Drew, A. Emili, D. W. Taylor, E. M. Marcotte, The protein organization of a red blood cell. *Cell Rep.* **40**, 111103 (2022).
28. V. L. Tzounakas, M. Dzieciatkowska, A. T. Anastasiadi, D. G. Karadimas, A. Vergaki, P. Siourounis, K. Stamoulis, I. S. Papassideri, A. G. Kriebardis, A. D'Alessandro, M. H. Antonelou, Red cell proteasome modulation by storage, redox metabolism and transfusion. *Blood Transfus.* **20**, 27–39 (2022).
29. L. J. Bruce, H. Guizouarn, N. M. Burton, N. Gabillat, J. Poole, J. F. Flatt, R. L. Brady, F. Borgese, J. Delaunay, G. W. Stewart, The monovalent cation leak in overhydrated stomatocytic red blood cells results from amino acid substitutions in the Rh-associated glycoprotein. *Blood* **113**, 1350–1357 (2009).
30. B. Fricke, A. C. Argent, M. C. Chetty, A. R. Pizzey, E. J. Turner, M. M. Ho, A. Iolascon, M. von Düring, G. W. Stewart, The "stomatin" gene and protein in overhydrated hereditary stomatocytosis. *Blood* **102**, 2268–2277 (2003).
31. U. Salzer, R. Zhu, M. Luten, H. Isobe, V. Pastushenko, T. Perkmann, P. Hinterdorfer, G. J. C. G. M. Bosman, Vesicles generated during storage of red cells are rich in the lipid raft marker stomatin. *Transfusion* **48**, 451–462 (2008).
32. Y. Zhu, C. Paszty, T. Turetsky, S. Tsai, F. A. Kuypers, G. Lee, P. Cooper, P. G. Gallagher, M. E. Stevens, E. Rubin, N. Mohandas, W. C. Mentzer, Stomatocytosis is absent in "stomatin"-deficient murine red blood cells. *Blood* **93**, 2404–2410 (1999).
33. M. M. Sedensky, M. A. Pujazon, P. G. Morgan, Tail clamp responses in stomatin knockout mice compared with mobility assays in *Caenorhabditis elegans* during exposure to diethyl ether, halothane, and isoflurane. *Anesthesiology* **105**, 498–502 (2006).
34. Z. Zhu, Z. Guo, X. Gao, Y. Chen, J. Huang, L. Li, B. Sun, Stomatin promotes neutrophil degranulation and vascular leakage in the early stage after severe burn via enhancement of the intracellular binding of neutrophil primary granules to F-actin. *Burns* **50**, 653–665 (2024).
35. H. Tao, K. Chen, Q. Wang, P. Zhu, M. Chu, W. Chen, C. Yang, Y. Gu, H. Yang, Q. Zhou, S. Lv, D. Geng, Targeting lipid raft-related stomatin to ameliorate osteoporosis in preclinical models. *Nat. Commun.* **16**, 5495 (2025).
36. V. Niggli, E. Carafoli, The plasma membrane Ca^{2+} ATPase: Purification by calmodulin affinity chromatography, and reconstitution of the purified protein. *Methods Mol. Biol.* **1377**, 57–70 (2016).
37. A. Cheng, C. Negro, J. F. Bruhn, W. J. Rice, S. Dallakyan, E. T. Eng, D. G. Waterman, C. S. Potter, B. Carragher, Leginon: New features and applications. *Protein Sci.* **30**, 136–150 (2021).
38. C. Suloway, J. Pulokas, D. Fellmann, A. Cheng, F. Guerra, J. Quispe, S. Stagg, C. S. Potter, B. Carragher, Automated molecular microscopy: The new Leginon system. *J. Struct. Biol.* **151**, 41–60 (2005).
39. A. Punjani, J. L. Rubinstein, D. J. Fleet, M. A. Brubaker, cryoSPARC: Algorithms for rapid unsupervised cryo-EM structure determination. *Nat. Methods* **14**, 290–296 (2017).
40. A. Punjani, H. Zhang, D. J. Fleet, Non-uniform refinement: Adaptive regularization improves single-particle cryo-EM reconstruction. *Nat. Methods* **17**, 1214–1221 (2020).
41. T. D. Goddard, C. C. Huang, E. C. Meng, E. F. Pettersen, G. S. Couch, J. H. Morris, T. E. Ferrin, UCSF ChimeraX: Meeting modern challenges in visualization and analysis. *Protein Sci.* **27**, 14–25 (2018).
42. E. F. Pettersen, T. D. Goddard, C. C. Huang, E. C. Meng, G. S. Couch, T. I. Croll, J. H. Morris, T. E. Ferrin, UCSF ChimeraX: Structure visualization for researchers, educators, and developers. *Protein Sci.* **30**, 70–82 (2021).
43. E. C. Meng, T. D. Goddard, E. F. Pettersen, G. S. Couch, Z. J. Pearson, J. H. Morris, T. E. Ferrin, UCSF ChimeraX: Tools for structure building and analysis. *Protein Sci.* **32**, e4792 (2023).
44. J. Jumper, R. Evans, A. Pritzel, T. Green, M. Figurnov, O. Ronneberger, K. Tunyasuvunakool, R. Bates, A. Žídek, A. Potapenko, Highly accurate protein structure prediction with AlphaFold. *Nature* **596**, 583–589 (2021).
45. E. F. Pettersen, T. D. Goddard, C. C. Huang, G. S. Couch, D. M. Greenblatt, E. C. Meng, T. E. Ferrin, UCSF Chimera—A visualization system for exploratory research and analysis. *J. Comput. Chem.* **25**, 1605–1612 (2004).
46. P. Emsley, K. Cowtan, Coot: Model-building tools for molecular graphics. *Acta Crystallogr. D Biol. Crystallogr.* **60**, 2126–2132 (2004).
47. P. V. Afonine, B. K. Poon, R. J. Read, O. V. Sobolev, T. C. Terwilliger, A. Urzhumtsev, P. D. Adams, Real-space refinement in PHENIX for cryo-EM and crystallography. *Acta Crystallogr. D Struct. Biol.* **74**, 531–544 (2018).
48. P. V. Afonine, B. P. Klaholz, N. W. Moriarty, B. K. Poon, O. V. Sobolev, T. C. Terwilliger, P. D. Adams, A. Urzhumtsev, New tools for the analysis and validation of cryo-EM maps and atomic models. *Acta Crystallogr. D Struct. Biol.* **74**, 814–840 (2018).

Acknowledgments: Cryo-EM data were collected at the Columbia Cryo-EM facility and at the Simons Electron Microscopy Center (SEMC), with assistance from staff at both SEMC and the Columbia University Cryo-Electron Microscopy Center. R. Grassucci and Z. Zhang from the Columbia Cryo-EM Center helped with data collection. We thank K. Kim for support. **Funding:** This study was supported by the National Institutes of Health (NIH) through grants R01-HL168178 (O.B.C.). The Irma T. Hirschl Trust provided support for O.B.C. **Author contributions:** Writing—original draft: F.V. and O.B.C. Conceptualization: F.V. and O.B.C. Investigation: F.V. and O.B.C. Writing—review and editing: F.V. and O.B.C. Methodology: F.V., T.C., O.B.C., and L.B. Resources: F.V., T.C., O.B.C., and L.B. Data curation: F.V., H.L., and O.B.C. Validation: F.V. and O.B.C. Supervision: F.V. and O.B.C. Formal analysis: F.V. and H.L. Project administration: F.V. and O.B.C. Visualization: F.V., H.L., and O.B.C. Funding acquisition: O.B.C. **Competing interests:** The authors declare that they have no competing interests. **Data, code, and materials availability:** All data and code needed to evaluate and reproduce the results in the paper are present in the paper and/or the Supplementary Materials. There are no new materials generated in the study. The cryo-EM density maps and models have been deposited in the Electron Microscopy Data Bank and the PDB. These are the IDs for the different cryo-EM data presented in table S1: stomatin C8 PDB (9Z7U) and EMDB (EMD-73881); AQP1 C4 PDB (9ZCZ) and EMDB (EMD-74046); UT-B C3 PDB (9ZD0) and EMDB (EMD-74047); AQP1 C1 PDB (9ZD2) and EMDB (EMD-74049); and stomatin intramembrane PDB (9ZD5) and EMDB (EMD-74052).

Submitted 9 September 2025
Accepted 26 February 2026
Published 1 April 2026
10.1126/sciadv.aec1721